

PAPER

## Bidirectional flow of action potentials in axons drives activity dynamics in neuronal cultures

To cite this article: JC Mateus *et al* 2021 *J. Neural Eng.* **18** 066045

View the [article online](#) for updates and enhancements.

### You may also like

- [Adding a single pulse into high-frequency pulse stimulations can substantially alter the following episode of neuronal firing in rat hippocampus](#)  
Yifan Hu, Zhouyan Feng, Lvpio Zheng et al.
- [Alteration of neural action potential patterns by axonal stimulation: the importance of stimulus location](#)  
Patrick E Crago and Nathaniel S Makowski
- [Randomized cortical stimulation could ameliorate locomotive inability in Parkinsonian rats: a pilot study](#)  
Rong-Chao Peng, Xiu-Xiu Liu, Ya Ke et al.



## PAPER

## Bidirectional flow of action potentials in axons drives activity dynamics in neuronal cultures

RECEIVED  
16 August 2021REVISED  
7 December 2021ACCEPTED FOR PUBLICATION  
10 December 2021PUBLISHED  
29 December 2021JC Mateus<sup>1,2,3</sup> , CDF Lopes<sup>1,2</sup> , M Aroso<sup>1,2</sup> , AR Costa<sup>1,4</sup>, A Gerós<sup>1,2,5</sup> , J Meneses<sup>6,7</sup>, P Faria<sup>6</sup>, E Neto<sup>1,2</sup> , M Lamghari<sup>1,2</sup> , MM Sousa<sup>1,4</sup> and P Aguiar<sup>1,2,\*</sup> <sup>1</sup> I3S—Instituto de Investigação e Inovação em Saúde, Universidade do Porto, Porto, Portugal<sup>2</sup> INEB—Instituto de Engenharia Biomédica, Universidade do Porto, Porto, Portugal<sup>3</sup> ICBAS—Instituto de Ciências Biomédicas Abel Salazar, Universidade do Porto, Porto, Portugal<sup>4</sup> IBMC—Instituto de Biologia Molecular e Celular, Universidade do Porto, Porto, Portugal<sup>5</sup> FEUP—Faculdade de Engenharia da Universidade do Porto, Porto, Portugal<sup>6</sup> CDRSP-IPL—Centre for Rapid and Sustainable Product Development—Instituto Politécnico de Leiria, Marinha Grande, Portugal<sup>7</sup> IBEB—Instituto de Biofísica e Engenharia Biomédica, Faculdade de Ciências, Universidade de Lisboa, Lisboa, Portugal

\* Author to whom any correspondence should be addressed.

E-mail: [pauloaguiar@ineb.up.pt](mailto:pauloaguiar@ineb.up.pt)**Keywords:** axonal electrophysiology, bidirectional axonal conduction, ectopic action potential, hippocampal neurons, dorsal root ganglia, microelectrode array, microfluidicsSupplementary material for this article is available [online](#)**Abstract**

**Objective.** Recent technological advances are revealing the complex physiology of the axon and challenging long-standing assumptions. Namely, while most action potential (AP) initiation occurs at the axon initial segment in central nervous system neurons, initiation in distal parts of the axon has been reported to occur in both physiological and pathological conditions. The functional role of these ectopic APs, if exists, is still not clear, nor its impact on network activity dynamics.

**Approach.** Using an electrophysiology platform specifically designed for assessing axonal conduction we show here for the first time regular and effective bidirectional axonal conduction in hippocampal and dorsal root ganglia cultures. We investigate and characterize this bidirectional propagation both in physiological conditions and after distal axotomy. **Main results.** A significant fraction of APs are not coming from the canonical synapse-dendrite-soma signal flow, but instead from signals originating at the distal axon. Importantly, antidromic APs may carry information and can have a functional impact on the neuron, as they consistently depolarize the soma. Thus, plasticity or gene transduction mechanisms triggered by soma depolarization can also be affected by these antidromic APs. Conduction velocity is asymmetrical, with antidromic conduction being slower than orthodromic. **Significance.** Altogether these findings have important implications for the study of neuronal function *in vitro*, reshaping our understanding on how information flows in neuronal cultures.

**1. Introduction**

A neuron is a highly specialized cell, typically compartmentalized into dendrites, soma, and the axon. The axon is often seen as a mere transmission cable for action potential (AP) propagation but this a very limiting view, partially arising from the technical challenges in recording from the thin axonal branches of vertebrate neurons [1, 2]. Recent breakthroughs, made possible by *in vitro* technological developments such as super-resolution microscopy

[3], voltage imaging [4], fluorescence-guided subcellular patch-clamp [5], microfluidic tools [6, 7], or microelectrode arrays (MEAs) [8] have opened new insights into axonal signal conduction and generated a renewed interest in axon physiology. Accordingly, accumulating evidence shows that the computational repertoire of the axon is much more complex than traditionally thought (for reviews see [1, 2, 9–11]).

After the seminal work by Hodgkin and Huxley on axonal propagation [12], the AP initiation and its propagation have been extensively investigated [11].

These studies have placed the axon initial segment (AIS) as the main site capable of AP generation in central nervous system (CNS) neurons. Intriguingly, several studies have demonstrated that APs generated at distal sites of the axon, also known as ectopic APs (EAPs), co-occur in diverse types of neurons both *ex vivo* and *in vivo* [13–19]. Such studies opened perspectives on neuronal communication beyond the canonical orthodromic signal transmission [9, 10]. In vertebrates, the occurrence of EAPs has been associated with pathological conditions where the axon is hyper-excitable (e.g. epilepsy, nerve injury, demyelination) [13, 20–22], but also with physiological functions, such as synaptic plasticity [17, 23], or fast network oscillations [14, 16, 19]. Still, as these studies relied on patch-clamp paired recordings, or paired field recordings from brain slices, the fine detection and characterization of the antidromic conduction properties (e.g. conduction velocity) could not be attained. Moreover, many uncertainties still hold regarding the precise mechanism(s) of EAPs' initiation [1, 10]. Hypotheses such as local depolarization mediated by activity in connected (e.g. axo-axonal coupling) [16, 24] or adjacent axons (ephaptic coupling) [25, 26], as well as stochastic activation of sodium channels in unmyelinated distal thin segments of the axon [13, 21] have been proposed, but the characterization and function of EAPs remain elusive. Importantly, it remains to be shown if EAPs/antidromic APs carry usable information to the cell body or if they are simply an electrophysiological glitch. From a functional perspective, a bidirectional flow of activity would certainly increase the complexity, but also the computational power of the axon [1]. Learning and plasticity studies in theoretical neuroscience have demonstrated the significant relevance of hypothetical mechanisms that could propagate signals (namely error signals) back to presynaptic neurons (for review see [27]). This is tightly related to the ideas behind the backpropagation algorithm [28], a central element in state-of-the-art artificial neuronal networks, such as deep neuronal networks.

In the peripheral nervous system, however, signal initiation and axonal conduction have different characteristics. *In vivo*, the peripheral process of sensory neurons generates APs distally, which propagate antidromically towards the dorsal root ganglia (DRG). The majority of *in vitro* studies have focused, however, on molecular processes, with no electrophysiological characterizations of axon physiology [29, 30]. Thus, it remains to be shown if cultured DRGs recapitulate the ability to generate APs at their distal terminals in both physiological and pathological contexts (e.g. after axotomy). This characterization should impact the use of DRG neuronal cultures in various contexts where signal conduction is thought to play a key role (e.g. axonal transport, axon regeneration).

Emerging technologies that allow probing axonal function with high temporal and spatial resolution can help characterize and understand EAPs/antidromic APs. We and others have combined microElectrode arrays and microFluidics ( $\mu$ EFs) to compartmentalize neuronal cultures in well-defined topologies that allow functional readouts [31–34], as well as selective manipulations of the different neuronal compartments [6, 35, 36]. In particular,  $\mu$ EFs allow the isolation of axons within microchannels, which are aligned over a set of micro-electrodes. Thus,  $\mu$ EFs allow for the detection of propagating axonal signals with very high fidelity and temporal resolution in long-term experiments, which are not possible with any other technique [31, 35].

Here, using  $\mu$ EFs and detailed temporal analysis, we report the consistent occurrence of bidirectional axonal conduction in two different *in vitro* models: dissociated hippocampal neurons and DRG organotypic cultures. Via a combination of extracellular electrophysiological recording/stimulation and fast calcium imaging, we show that evoked antidromic events effectively depolarize the soma, anticipating functional roles of antidromic activity. Addressing this frequent occurrence of antidromic APs in both hippocampal and DRG cultures, we explore possible functional roles of these signals under two different conditions: in the pathological context of axonal lesions, we show that EAPs occur after distal axotomy; additionally, we show that physiological changes in the biochemical environment of the distal axon can promote antidromic activity. Finally, we report differences in the velocity of signal propagation, with antidromic conduction being slower than orthodromic.

## 2. Results

### 2.1. Tracking signal propagation reveals a bidirectional flow of activity

In this study, we improved on our previous microfluidic chamber design [31, 33], by optimizing it for the study of axonal function (details in the section 4). Importantly, we set the number of microchannels to match the number of microelectrode columns, so that every microchannel would be probed electrophysiologically. The alignment of this microfluidic chamber with 252-electrode MEAs allowed for the probing of 16 microchannels, encompassing seven microelectrodes each, per experiment (figure 1(A)). This configuration enabled the separation of somal and axonal activity within the same experiment (figure 1(B)). The higher impedance within the microchannels greatly amplifies the otherwise difficult-to-detect axonal signals [31, 37]. Due to the increase in signal-to-noise ratio (SNR), the mean firing rate (MFR) (figures 1(C)–(E)) and the percentage of consistently active microelectrodes

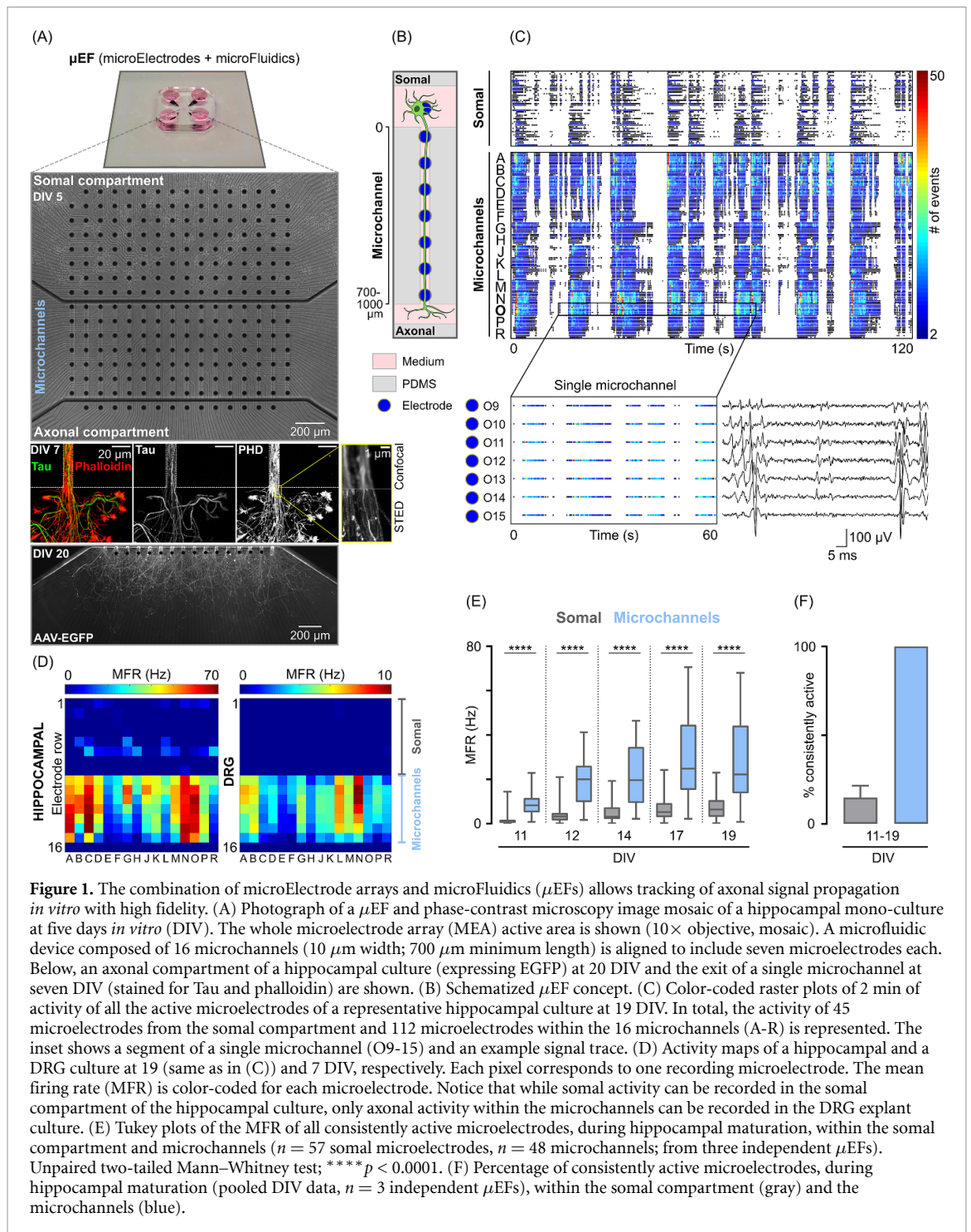


(figure 1(F)) were significantly higher within the microchannels.

In the used configuration, single-compartment neuronal cultures (mono-cultures), somata were maintained in a somal compartment and extended their axons along the microchannels to a pure axonal compartment (figures 1(A) and (B)). We investigated axonal function in two different *in vitro* models: dissociated hippocampal neurons and organotypic cultures of DRG. These different models exhibited marked differences in axonal outgrowth and electrophysiological maturation. Hippocampal neurons'

axons grew through the microchannel within five to seven days (figure 1(A)), while DRG axons took three to five days. Unlike mature hippocampal neurons, DRG neurons did not fire in bursts but rather exhibited sporadic spontaneous activity. In physiological conditions, this relatively low level of activity also occurs *in vivo* [29]. As DRG explants were placed outside the MEA active area, activity was only recorded in the microchannels (figure 1(D)). This further highlights the importance of microchannels to record axonal activity extracellularly.

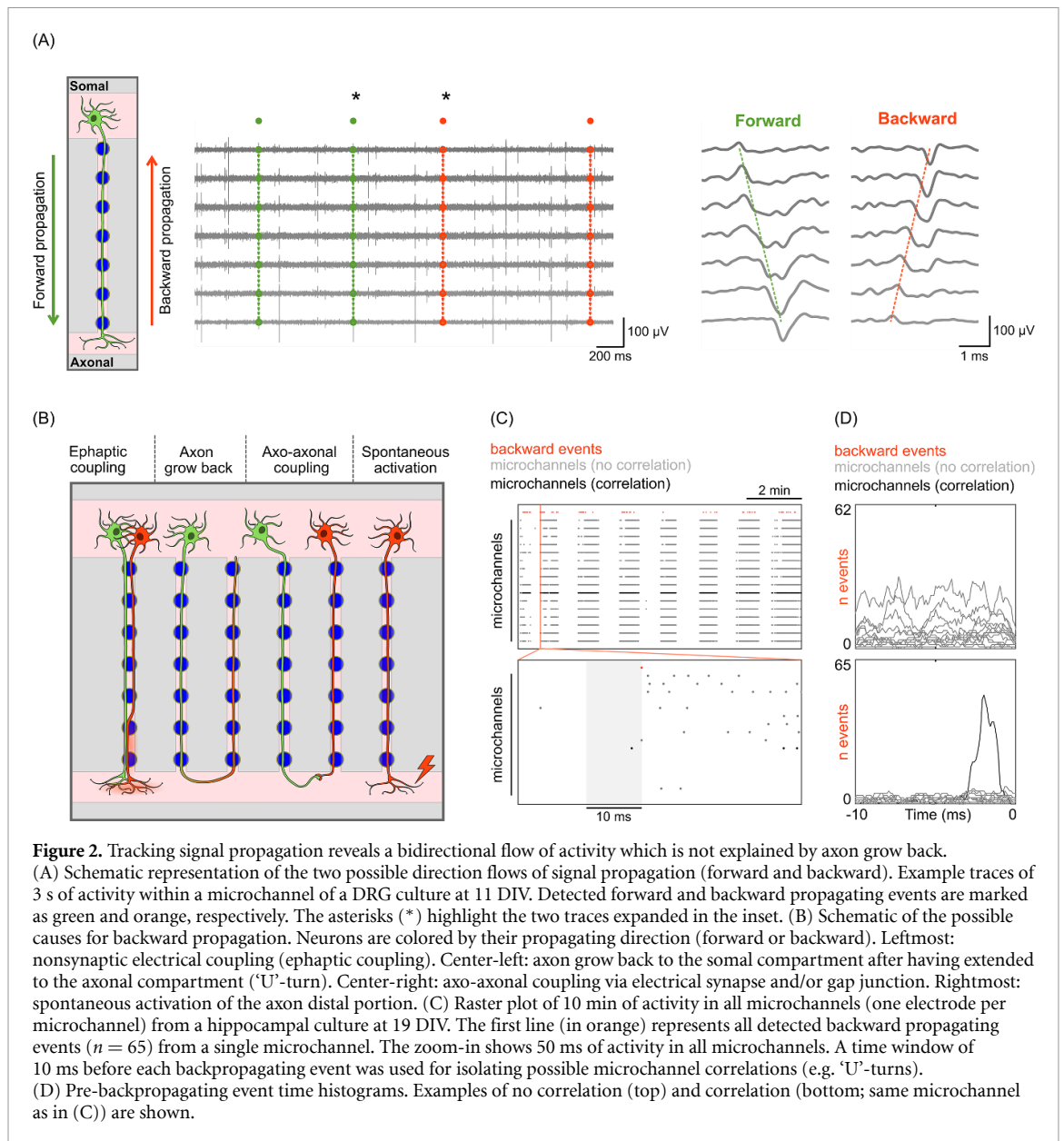


**Figure 2.** Tracking signal propagation reveals a bidirectional flow of activity which is not explained by axon grow back. (A) Schematic representation of the two possible direction flows of signal propagation (forward and backward). Example traces of 3 s of activity within a microchannel of a DRG culture at 11 DIV. Detected forward and backward propagating events are marked as green and orange, respectively. The asterisks (\*) highlight the two traces expanded in the inset. (B) Schematic of the possible causes for backward propagation. Neurons are colored by their propagating direction (forward or backward). Leftmost: nonsynaptic electrical coupling (ephaptic coupling). Center-left: axon grow back to the somal compartment after having extended to the axonal compartment ('U'-turn). Center-right: axo-axonal coupling via electrical synapse and/or gap junction. Rightmost: spontaneous activation of the axon distal portion. (C) Raster plot of 10 min of activity in all microchannels (one electrode per microchannel) from a hippocampal culture at 19 DIV. The first line (in orange) represents all detected backward propagating events ( $n = 65$ ) from a single microchannel. The zoom-in shows 50 ms of activity in all microchannels. A time window of 10 ms before each backpropagating event was used for isolating possible microchannel correlations (e.g. 'U'-turns). (D) Pre-backpropagating event time histograms. Examples of no correlation (top) and correlation (bottom; same microchannel as in (C)) are shown.

We found that in experiments using either dissociated hippocampal neurons or DRG explants' monocultures, a significant number of events propagated from the axonal to the somal compartment—backward propagation (figure 2(A)). This backward propagation completely ceased after selectively adding tetrodotoxin (TTX) to the axonal compartment ( $n = 6$  independent  $\mu$ EFs) (supplementary figure S1 (available online at [stacks.iop.org/JNE/18/066045/mmedia](https://stacks.iop.org/JNE/18/066045/mmedia))), supporting the hypothesis that the observed activity initiates in the axonal compartment.

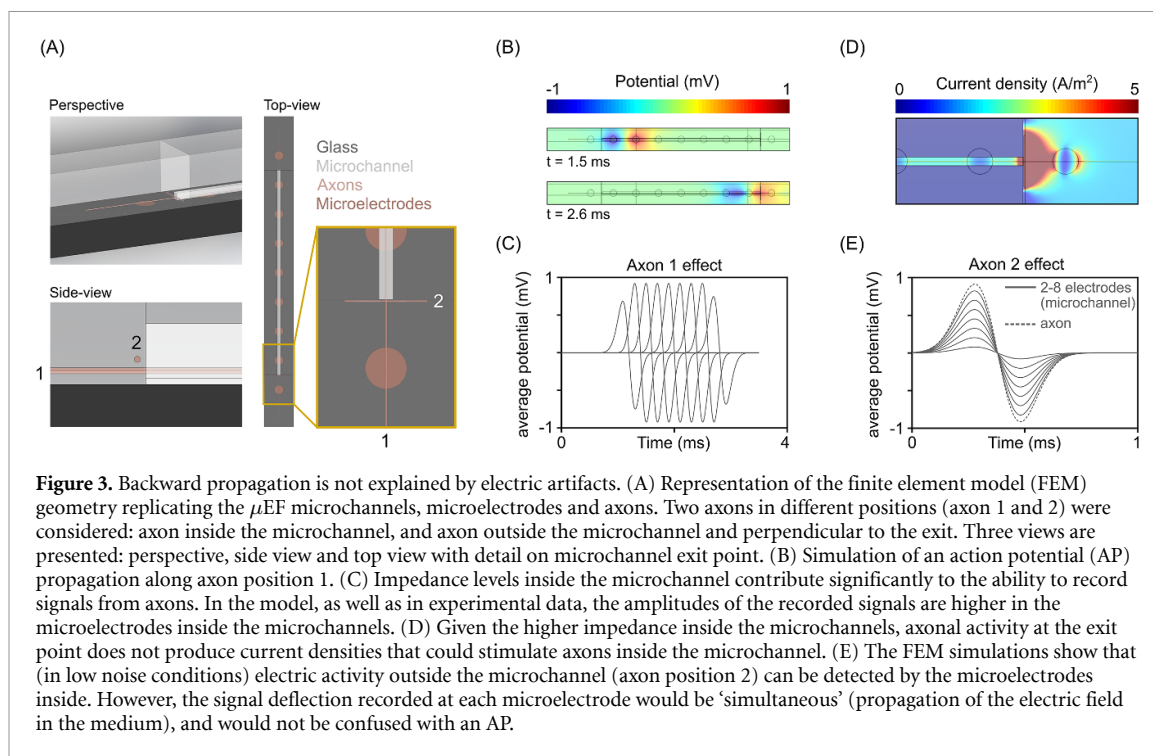
Different causes can support the observed backward propagation (figure 2(B)). First, the simple case of an axon growing back to the somal compartment after having extended to the axonal compartment ('U'-turn). Additionally, although axons do not find dendritic targets in the axonal compartment, they may establish axo-axonal synapses and/or couple via gap junctions [24], so that one axon conducts APs

orthodromically and the other antidromically along the microchannels. Alternatively, very close proximity between axons in the axonal compartment, combined with high electrical coupling conditions, can originate ephaptic coupling [25] where, as with gap junctions or axo-axonic connections, an axon conducts APs antidromically. Finally, this activity may arise from APs initiation caused by activation of sodium channels (stochastic, or not) at the axon distal end followed by antidromic propagation [13, 21]. The possible origin of the backward propagation was dissected through a set of experiments that selectively manipulated the axonal compartment.

## 2.2. Backward propagation is not explained by returning axons nor $\mu$ EF electric artifacts

The  $\mu$ EF design did not prevent axons from growing back to the somal compartment after reaching the axonal compartment ('U'-turns), though these axons





would have to elongate for, at least, 1.5 mm. Thus, we tested if the detected backward propagation could simply be caused by axon grow back (figure 2(B)). As the AP activity in returning axons would be temporally correlated with AP activity in another microchannel, we performed time-delay analysis of the backward propagation events against the preceding AP activity in all microchannels (figure 2(C)).

For hippocampal neurons at 11 and 19 DIV ( $n = 5$  independent  $\mu$ EFs), only a minority (<10%) of the microchannels where backward propagating events were detected showed temporal correlations (within 10 ms) with AP activity in other microchannels. An example of neighboring microchannels with a strong temporal correlation is shown in figure 2(D). In DRG experiments at six DIV ( $n = 5$  independent  $\mu$ EFs), we found a single pair of temporally correlated microchannels. Moreover, we could not detect a correlation within the same microchannel in any experiment. Thus, the great majority of the detected backward propagation does not emerge from axon grow back to the somal compartment after a 'U'-turn. Similarly, the obtained time-delay distributions do not favor the hypotheses of strong axo-axonal or ephaptic coupling as a major cause for the detected backward propagating activity.

A last, but not less relevant alternative hypothesis for the observed backward propagation signals is the presence of electric artifacts in the  $\mu$ EF microchannels. Detailed simulations using finite element model (FEM), recreating the core geometrical elements of the microchannels (figure 3(A)), were carried out to assess two situations that could be incorrectly interpreted as a backward propagation signal: (a)

complex electrical behaviors driven by the extracellular currents of forward APs, and (b) influence of axonal activity at the exit of the microchannels on the readout of the microelectrodes. The microchannels' small cross-section leads to higher impedances and increased recorded signal amplitudes, in accordance with the experimental data (figures 3(B) and (C)). However, the forward propagation of APs inside the microchannels does not generate any unexpected potential readings at the microchannel extremities that could trigger another AP (Supplementary Movie 1). The increased impedance inside the microchannels is also responsible for the fact that axonal electrical activity just outside the microchannel does not generate relevant electrical potential/currents that could trigger an AP in an axon inside the microchannel (i.e. the microchannels do not 'channel in' outside currents) (figure 3(D)). Finally, the FEM model also excludes the possibility of axonal activity at the exit point of the microchannel being picked up by the microelectrodes inside and incorrectly interpreted as a backward propagation signal. In such case, not only the signal amplitudes in the microelectrodes further away would be extremely low, the signal deflection in all electrodes would be virtually synchronous (as we would be recording the electric disturbance in the medium and not a traveling wave in an axon) (figure 3(E)).

Concluding, since the vast majority of the detected backward propagating activity does not come from axons growing back, nor electrical artifacts at microchannel entrance, the origin is necessarily the distal parts of the axons. As such, the terminology backward propagation will be replaced

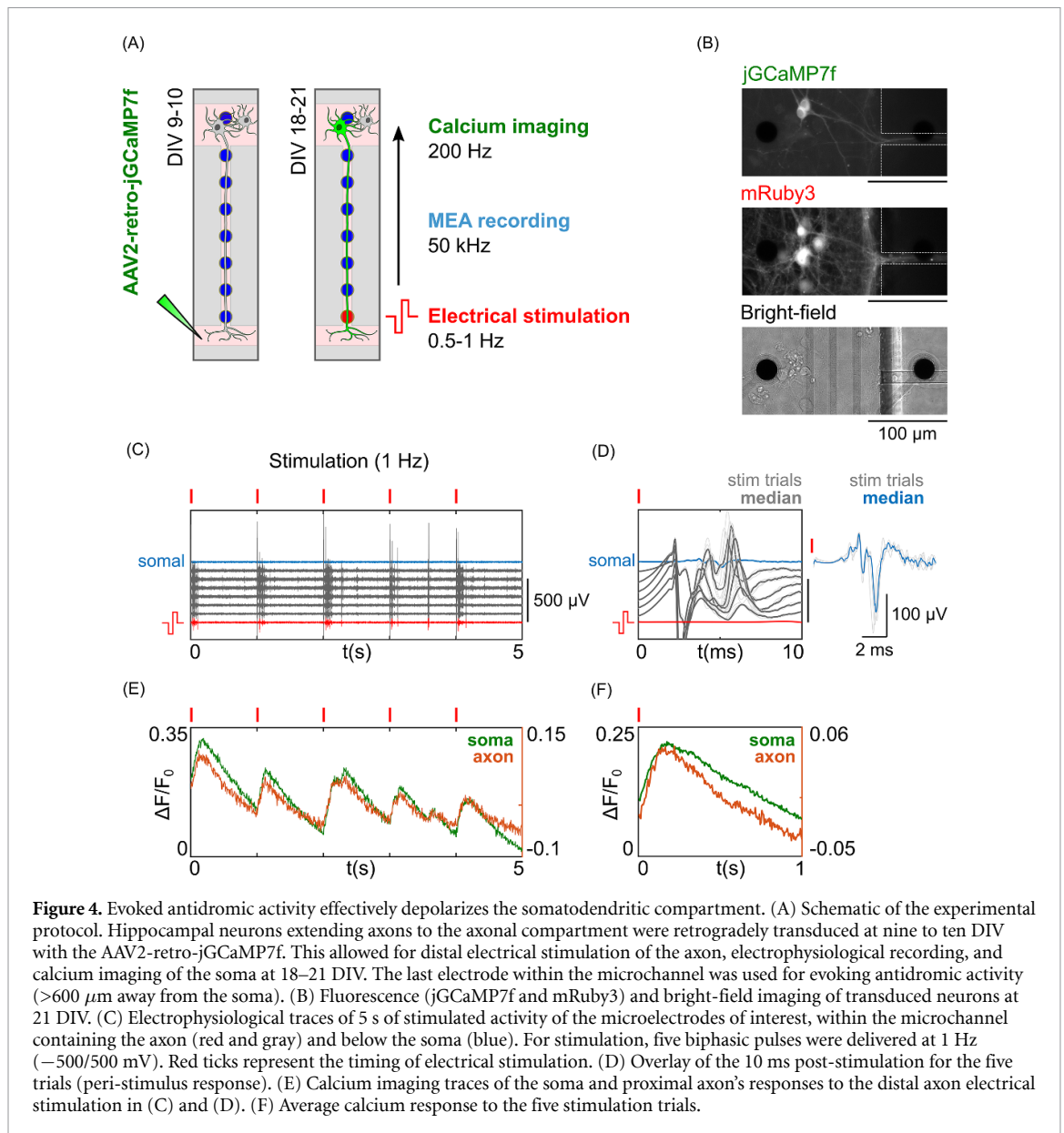


**Figure 4.** Evoked antidromic activity effectively depolarizes the somatodendritic compartment. (A) Schematic of the experimental protocol. Hippocampal neurons extending axons to the axonal compartment were retrogradely transduced at nine to ten DIV with the AAV2-retro-jGCaMP7f. This allowed for distal electrical stimulation of the axon, electrophysiological recording, and calcium imaging of the soma at 18–21 DIV. The last electrode within the microchannel was used for evoking antidromic activity (>600  $\mu\text{m}$  away from the soma). (B) Fluorescence (jGCaMP7f and mRuby3) and bright-field imaging of transduced neurons at 21 DIV. (C) Electrophysiological traces of 5 s of stimulated activity of the microelectrodes of interest, within the microchannel containing the axon (red and gray) and below the soma (blue). For stimulation, five biphasic pulses were delivered at 1 Hz ( $-500/500$  mV). Red ticks represent the timing of electrical stimulation. (D) Overlay of the 10 ms post-stimulation for the five trials (peri-stimulus response). (E) Calcium imaging traces of the soma and proximal axon's responses to the distal axon electrical stimulation in (C) and (D). (F) Average calcium response to the five stimulation trials.

by antidromic conduction for the remainder of the manuscript.

### 2.3. Antidromic APs effectively depolarize the soma

For EAPs/antidromic APs to carry usable information to the cell body and have a functional in CNS neurons, they should reach and effectively depolarize the soma. Thus, we tested if eliciting antidromic activity could lead to soma depolarization. For that, we retrogradely transduced hippocampal mono-cultures with adeno-associated virus (AAV)2-retro-jGCaMP7f at nine to ten DIV, which allowed us to perform calcium imaging of neurons extending to the axonal compartment (figure 4(A)). This AAV2-retro variant [38] allows for the robust retrograde expression of the protein of interest. Here, we used it to selectively induce the expression of jGCaMP7f ('fast'), a genetically encoded calcium indicator with fast kinetics and single-AP sensitivity [39]. As relatively few

neurons project axons to the axonal compartment, labeling was sparse even weeks post-transduction (figure 4(B)).

A standard electrical stimulation protocol was used to elicit antidromic activity on transduced neurons (18–21 DIV), while performing fast calcium imaging and electrophysiological recording (figure 4(A)). For that, five electrical pulses were delivered to the last microelectrode within the microchannel of interest (at least 600  $\mu\text{m}$  away from the soma) per trial. The microchannel of interest (i.e. containing the axon of the transduced neuron) could be readily identified via labeling (mRuby3 and/or jGCaMP7f) (figure 4(B)). Antidromic APs were elicited reliably for the range of tested stimulation amplitudes ( $-0.5/0.5$  to  $-1.0/1.0$  V) and frequencies (0.5–1 Hz) (figure 4(C) and Supplementary Figure S2). The resulting stimulation artifact precluded the electrophysiological recording of the immediate responses

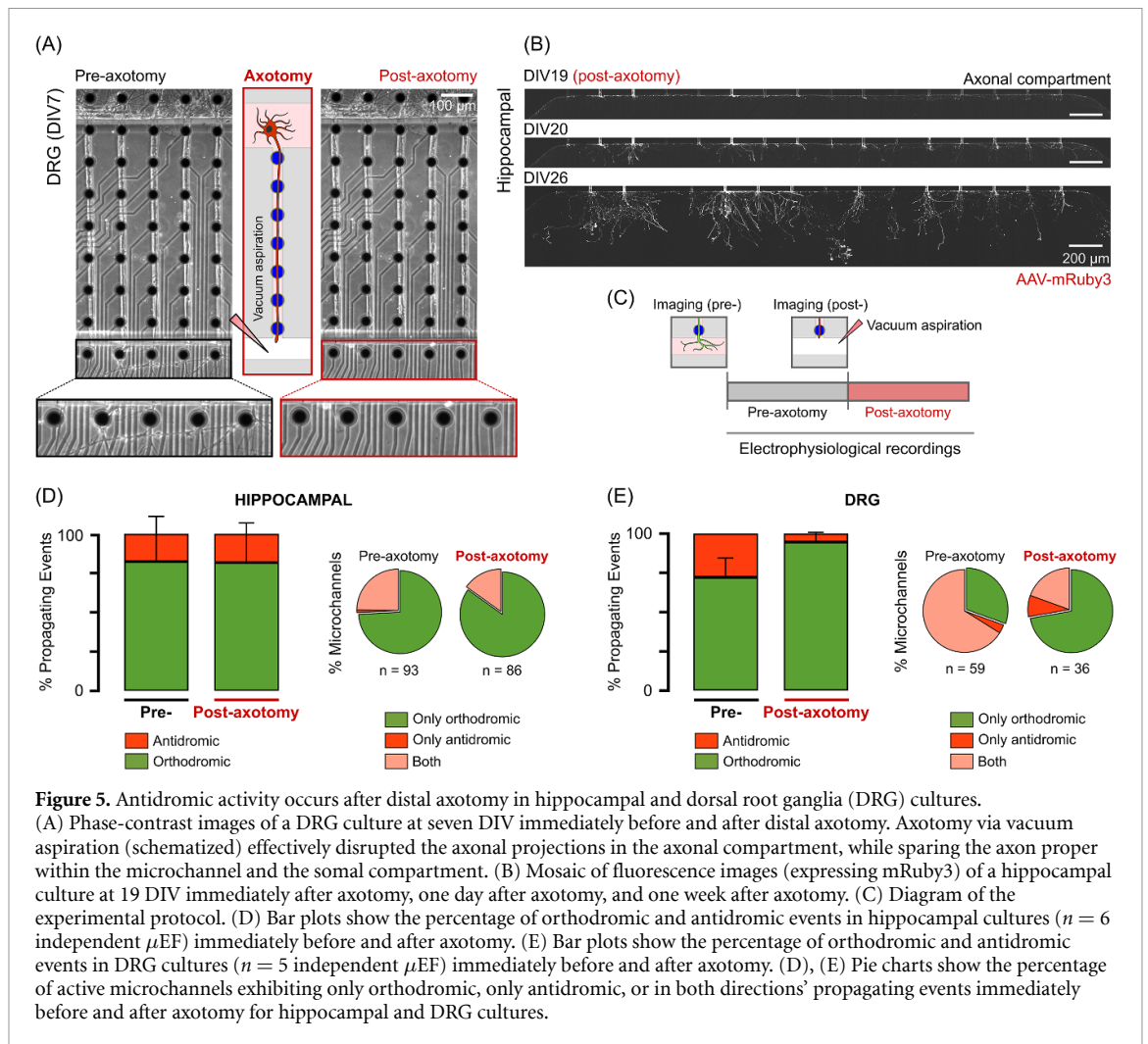


**Figure 5.** Antidromic activity occurs after distal axotomy in hippocampal and dorsal root ganglia (DRG) cultures. (A) Phase-contrast images of a DRG culture at seven DIV immediately before and after distal axotomy. Axotomy via vacuum aspiration (schematized) effectively disrupted the axonal projections in the axonal compartment, while sparing the axon proper within the microchannel and the somal compartment. (B) Mosaic of fluorescence images (expressing mRuby3) of a hippocampal culture at 19 DIV immediately after axotomy, one day after axotomy, and one week after axotomy. (C) Diagram of the experimental protocol. (D) Bar plots show the percentage of orthodromic and antidromic events in hippocampal cultures ( $n = 6$  independent  $\mu$ EF) immediately before and after axotomy. (E) Bar plots show the percentage of orthodromic and antidromic events in DRG cultures ( $n = 5$  independent  $\mu$ EF) immediately before and after axotomy. (D), (E) Pie charts show the percentage of active microchannels exhibiting only orthodromic, only antidromic, or in both directions' propagating events immediately before and after axotomy for hippocampal and DRG cultures.

(within 5 ms post-stimuli) along the microchannel. However, somal depolarizations could be recorded when neurons were near a somal microelectrode (figure 4(D)).

Somatodendritic depolarizations were consistently obtained in response to evoked antidromic APs, as can be seen in the calcium imaging traces (figures 4(E) and (F) and S2) (supplementary movies 2 and 3). These results were reproduced in several neurons from six independent  $\mu$ EFs at 18–21 DIV. With antidromic APs being able to carry information and effectively depolarizing the soma (potentially triggering, for example, protein translation or plasticity mechanisms), the following sections address different physiological contexts capable of triggering/modulating antidromic activity.

#### 2.4. Antidromic APs occur after distal axotomy

Spontaneous EAP generation has been shown to occur following axonal injury [13, 20]. Here, we studied the effect of axon lesions on the generation of antidromic signaling. Taking advantage of the high fluidic resistance between compartments, we could subject neurons to distal axotomy  $>700 \mu\text{m}$  away from their undisturbed somata. This procedure

effectively disrupted axonal projections in the axonal compartment, while sparing the axon proper within the microchannel (figures 5(A) and (B)), mimicking the conditions of severe axonal lesions [40]. Both before and following axotomy we recorded the spontaneous axonal activity of hippocampal and DRG cultures (figure 5(C)). We will refer to microchannels in which propagating events were detected as 'active microchannels'.

#### 2.5. Hippocampal neurons

Distal axotomy in hippocampal cultures has been explored in different contexts, including in *in vitro* models for post-traumatic epilepsy [40], an established complication from traumatic brain injury. After axotomy the antidromic events are expected to be triggered at the injury site (figure 5(B)). We studied the electrophysiological effects of distal axotomy in mature hippocampal cultures (18–20 DIV,  $n = 6$  independent  $\mu$ EF). Before axotomy, 26% of the active microchannels (24 out of 93) exhibited antidromic activity, while immediately after axotomy, only 15% of the active microchannels (13 out of 86) exhibited antidromic activity. The average number of detected propagating events per minute



decreased immediately after axotomy (reduction of  $45.6 \pm 17.6\%$ ). Still, the fraction of antidromic events was similar before and after axotomy (figure 5(D)).

## 2.6. DRG explants

In sensory neurons *in vivo*, spontaneous AP generation at the site of axonal injury is an important generator of pathological conditions, such as neuropathic pain [41]. However, in acute *ex vivo* whole DRG preparations (after lesion), EAPs are rarely encountered, as activity originates primarily in the soma. Typically, ectopic activity needs to be facilitated by applying  $K^+$  blockers to the recording bath [42]. Here we studied the effects of distal axotomy on the antidromic initiation of organotypic DRG cultures at seven DIV ( $n = 5$  independent  $\mu$ EF). Since most spontaneous axonal activity in DRGs *in vitro* is orthodromic, we analyzed here if ectopic/antidromic activity would emerge after lesion in DRG axon's distal end (figure 5(A)). DRG cultures exhibited a relevant percentage of antidromic events ( $24.2 \pm 13.7\%$ ) before axotomy (figure 5(D)). We detected antidromic activity in 70% (41 out of 59) of the active microchannels. Immediately after axotomy, we observed a great decrease in the average number of detected propagating events per minute (reduction of  $79.0 \pm 35.7\%$ ). We detected a much smaller fraction of antidromic events after axotomy ( $6.7 \pm 5.7\%$ ), which originated from 28% (10 out of 36) of the active microchannels. These results suggest that, while intact, *in vitro* DRG axons generate and conduct antidromic activity; however, immediately after axotomy, although many injured axons are silent, some antidromic activity occurs.

Overall, these results show that EAPs/antidromic activity occur after distal axotomy in both hippocampal and DRG cultures. Most probably, this activity is the result of AP initiation at the compromised axonal membrane (figures 5(A) and (B)). After axotomy, axons may degenerate or, instead, undergo a cytoskeletal reorganization (e.g. axon blebs, neuromas), which affects sodium channel dynamics. The consequences of this reorganization in EAP generation and function require further investigation.

## 2.7. Modulation of DRG explants' antidromic activity with osteoclast's conditioned medium (CM)

Previous studies have shown that osteoclastic activity produces changes in the biochemical microenvironment that activate the nociceptors of the innervating DRG nerve terminals [43]. We took advantage of the  $\mu$ EF's fluidic compartmentalization to selectively stimulate DRG axons with the secretome of osteoclasts cultured in mineralized substrates (active-resorbing osteoclasts) (figure 6(A)). We have previously reported that axonal stimulation with osteoclast's CM greatly increases the overall levels of axonal activity of DRG explants at six to seven

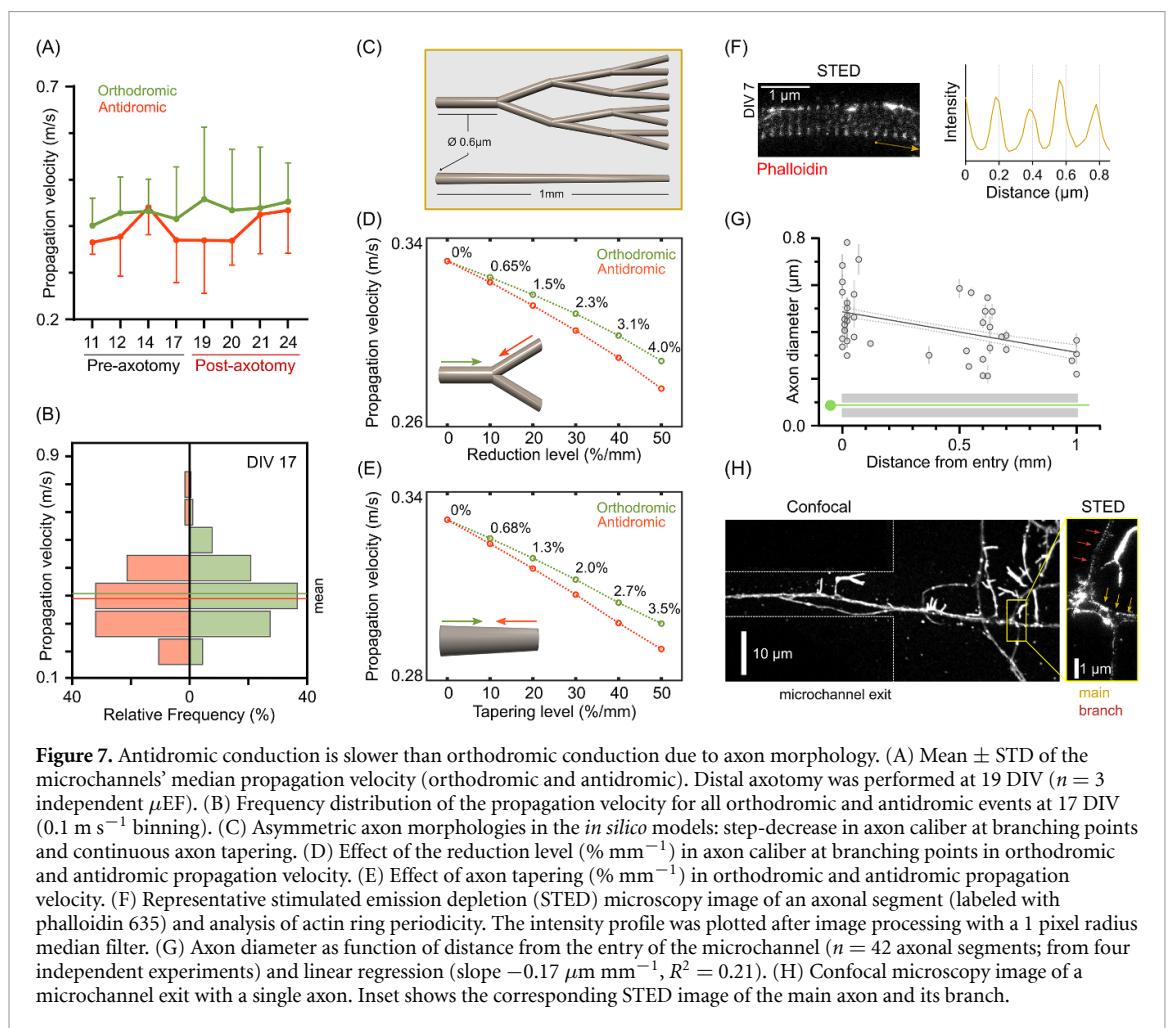
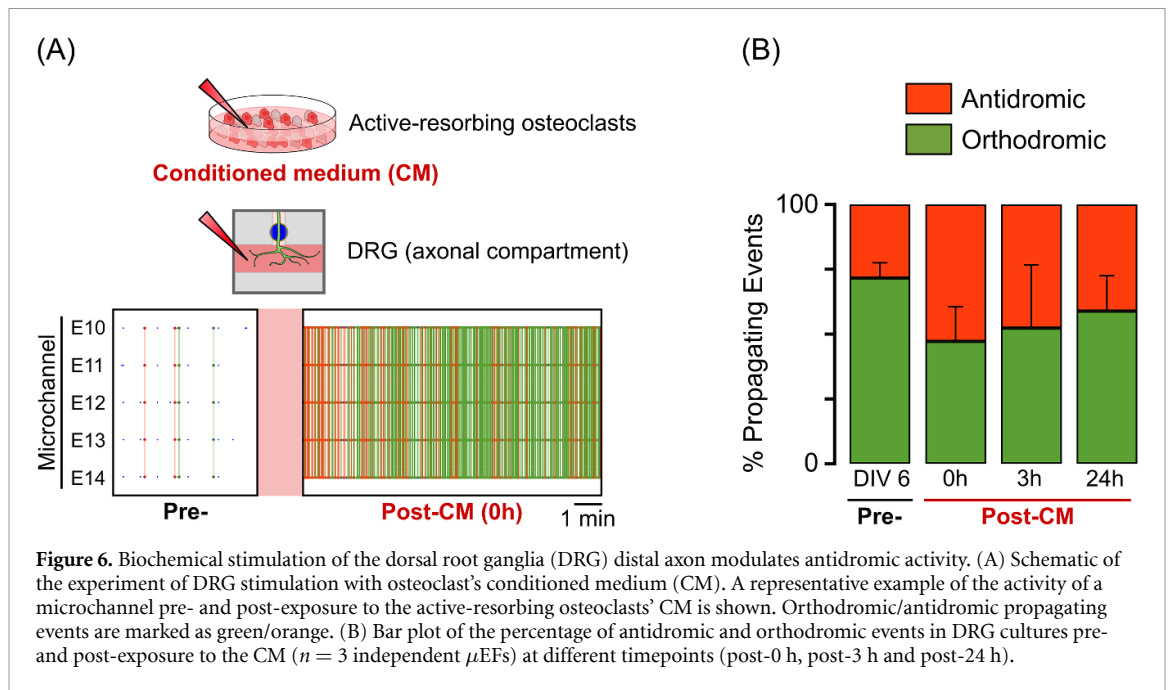
DIV [36], without assessing conduction direction. Here, we tested if this increase in axonal activity level was accompanied by an increase in the fraction of antidromic activity.

At six DIV, DRG cultures exhibited a relatively low fraction of antidromic events ( $28.4 \pm 5.9\%$ ,  $n = 3$  independent  $\mu$ EFs). Immediately after distal axonal stimulation with osteoclast's CM, this fraction increased to  $52.8 \pm 13.4\%$ . The following recording time points (3 h and 24 h post-CM) showed a tendency for this fraction to return to baseline levels, which may be the result of CM's metabolization. At seven DIV (24 h post-CM), the fraction of antidromic events was  $41.1 \pm 13.6\%$  (figure 6(B)). These results indicate that distal axon stimulation with osteoclast's CM can boost the initiation of antidromic activity. Importantly, by modulating antidromic initiation in a more physiologically relevant model than commonly used chemical stimulants (e.g. KCl), these results also show that  $\mu$ EFs may be used to study the physiological generation and function of antidromic activity in DRG cultures.

## 2.8. Conduction velocity is asymmetric

AP conduction along the axon is a tightly regulated and modulated process [11]. Biophysical parameters of the membrane [44], variations in axon diameter [3, 45], or ion channel densities and kinetics [46] greatly influence axonal conduction velocity. Here, the high-temporal resolution ( $20 \mu$ s at 50 kHz) of the  $\mu$ EF recordings allowed for the precise calculation and comparison of propagation velocity between orthodromic and antidromic APs (details in the section 4).

In hippocampal cultures ( $n = 3$  independent  $\mu$ EFs) we observed a moderate increase in propagation velocity along maturation in both orthodromic and antidromic events (figures 7(A) and (B)). At 11 DIV the average propagation velocity per microchannel was of  $0.40 \pm 0.06 \text{ m s}^{-1}$  (orthodromic) and  $0.37 \pm 0.03 \text{ m s}^{-1}$  (antidromic), while at 24 DIV (after axotomy at 19 DIV) it had increased to  $0.45 \pm 0.08 \text{ m s}^{-1}$  (orthodromic) and  $0.43 \pm 0.09 \text{ m s}^{-1}$  (antidromic). The orthodromic propagating velocity values were very consistent with previous results obtained from unmyelinated hippocampal neurons [34, 47, 48]. However, antidromic events were generally slower than orthodromic events (figures 7(A) and (B)). This can be observed in the trend of the microchannels' average propagation velocity (figure 7(A)) and in the shift in the velocities distributions (figure 7(B)). Although, the difference was as large as 21.3% at 19 DIV (immediately after axotomy), in physiological conditions the difference was below 10%. Propagation velocity for both orthodromic and antidromic events was not correlated with the microchannel's MFR (Pearson's correlation,  $p = 0.49$ ,  $p = 0.31$ , respectively), thus was



independent of spontaneous firing frequency within the microchannel.

We used the NEURON simulation environment to test the hypothesis if asymmetry in the

axon's morphology could explain the observed difference. We implemented models to test two different axon morphologies capable of generating asymmetric electrotonic lengths: continuous axon tapering, and

step-decreases in axon diameter at branching points (figure 7(C)). We observed that both axon morphologies introduced differences in antidromic and orthodromic conduction velocity, even for mild values of axon diameter reduction after branching or axonal tapering (figures 7(D) and (E)). The velocity difference was as high as 4%, at 50%  $\text{mm}^{-1}$  diameter reduction.

Beyond the well-described tapering in the soma-to-axon proper transition, little is known on how axon diameter changes along its length [49]. We performed stimulated emission depletion (STED) microscopy of axons growing along microchannel patterns to understand if the average hippocampal axon diameter could vary along the microchannel length (up to 1 mm). For the unequivocal identification of axons, we relied on specific staining (Tau antibody) and the presence of periodic ( $\approx 190$  nm) actin rings (figure 7(F)), a characteristic cytoskeleton organization [50, 51].

Analysis of different axonal segments at six to seven DIV ( $n = 42$ ) revealed that axon diameter correlated negatively with distance from the entry of the microchannel pattern (Pearson's correlation coefficient  $r = -0.46$ ) (figure 7(G)). The linear regression slope represented a 28–43%  $\text{mm}^{-1}$  (95% confidence interval) decrease in diameter. In some cases, we could measure the diameter of both the main axon and its thinner branch (figure 7(H)). The reduction in diameter at these branching points ranged from 15% to 53% ( $n = 5$  main axon/branch pairs). In summary, STED analysis confirmed the possibility of tapering levels and/or diameter reduction after branching in the order of 40%–50%  $\text{mm}^{-1}$ . Thus, the difference in antidromic and orthodromic conduction velocity may originate, at least partially, from these morphological conditions.

### 3. Discussion

The characterization and understanding of EAPs/antidromic activity have been limited by the technical difficulties of performing electrophysiology in the very thin mammalian axons. In this study, we made use of a powerful combination of methodologies (MEAs and microfluidics) to surpass important technical challenges. This setup allowed us to compartmentalize neuronal cultures and record spontaneous axonal signal conduction events with very high SNR and temporal resolution. Remarkably,  $\mu\text{EF}$  recordings of different mono-culture *in vitro* models revealed the unforeseen presence, and significant prevalence, of antidromic APs. These events could not be explained by returning axons ('U'-turns), nor  $\mu\text{EF}$  electric artifacts, and were completely abolished after selectively adding TTX to the axonal compartment. These results support the hypothesis of distal initiation of APs in neuronal cultures. Importantly, distal electrical stimulation of hippocampal neurons'

axons consistently led to somatodendritic depolarization, which suggests that antidromic activity may affect neuronal function. We observed similar results with DRG explants that, *in vitro*, show very different axonal conduction characteristics than what is expected from afferent sensory neurons *in vivo*.

To date, most studies using  $\mu\text{EF}$ s to address axonal function have employed dual-compartment (or co-culture) neuronal cultures of CNS neurons, where signal transmission was assumed to travel orthodromically from the supposed compartment of origin [35, 37, 52]. Moreover, in the few studies where neurons were seeded in a single compartment, the event detection methods assumed orthodromic propagation from the soma to the axonal compartment [32, 34]. Previous studies using dissociated DRG neurons have elicited APs via electrical stimulation [53], or capsaicin/KCl application [54], but to the best of our knowledge, no study has previously attempted to characterize the spontaneous signal conduction of DRG cultures. Our data shows clearly that bidirectional axonal conduction must be considered when analyzing functional data from both hippocampal and DRG cultures.

Regarding potential functional roles in physiological states, EAP generation at the distal portions of hippocampal neurons' axons has been reported in studies using *ex vivo* and *in vivo* models, particularly during sharp-wave ripple complexes [15–17, 19]. Interestingly, EAP generation is susceptible to conventional synaptic modulation, as somatic excitatory or inhibitory input can facilitate or suppress EAP generation, respectively [18]. Still, it is not understood in which conditions can EAPs depolarize the soma and have physiological functions. *Ex vivo* studies have shown that backpropagation of EAPs during gamma oscillations can be inhibited by axo-axonic interneurons that target the AIS of CA3 hippocampal neurons [14]. Yet, antidromic activity of CA1 hippocampal axons has been shown to reduce synaptic strength and lead to a widespread downscaling of upstream synaptic weights. Conversely, subsequent synaptic stimulation led to long-lasting synaptic potentiation [17]. More recently, the same authors associated antidromic activity with a rapid downregulation of brain-derived neurotrophic factor mRNA levels [23], a protein critically involved in canonical forms of synaptic plasticity. Ultimately, these studies suggest that orthodromic and antidromic activity may differentially regulate synaptic plasticity and gene expression. Regarding DRGs *in vitro*, we found that orthodromic conduction dominates, but antidromic activity can be elicited by the modulation of the electrophysiological environment of the distal axons. Using a physiologically relevant model of the innervated bone microenvironment [36, 43], we showed an increase in antidromic activity following distal axon stimulation with osteoclasts' CM. Nonetheless, further studies are required to unveil the mechanisms

behind AP triggering at the distal axons and the prevalence of axons that present bidirectional conduction. Future technologies, ideally capable of isolating single neurons and axons, may help decipher how EAPs arise and what is their function at different scales (from single-cell to network level).

In pathological conditions, we have explored the effects of distal axotomy in hippocampal neurons, as in a model for traumatic brain injury [40], and found that EAP/antidromic activity occurs after axonal lesion. With DRGs, spontaneous electrical activity and fraction of ectopic activity were diminished immediately after axotomy. *In vivo*, injured sensory neurons exacerbate the natural antidromic activity, a mechanism thought to be an originator of neuropathic pain [41], but silencing following peripheral injury also occurs and it has been proposed as a necessary trigger for axon regeneration [55]. Likewise, in acute *ex vivo* preparations, EAPs are rarely encountered after lesion, as APs originate primarily in the soma [42]. Still, the short- and long-term effects of axotomy in DRG axonal function should be the subject of further research, and future *in vitro* studies should explore ways of better mimicking the post-lesion axon environment.

Further characterization of the bidirectional signal conduction with high-temporal resolution recordings revealed an asymmetry in conduction velocity. This difference could be replicated in computational models of two symmetry breaking morphologies: axon tapering and diameter reduction at branching points. It is not clear however, if the asymmetry in conduction velocity has functional implications *per se*.

Taken together, our results reshape our understanding on how information flows in neuronal cultures by showing that EAPs/antidromic conduction occur in *in vitro* models of hippocampal and DRG neurons. Several studies have tried to impose unidirectional outgrowth of axons via complex physical/chemical patterning (reviewed in [7, 56]). Our study suggests that unidirectional axonal outgrowth may not necessarily lead to unidirectional information flow, a finding with important implications for the 'brain-on-chip' field. It remains to be shown if these reported mechanisms hold for *in vivo* conditions, but with *in vitro* models being used extensively in conditions where network dynamics play an important role (e.g. plasticity, neuronal circuits), acknowledging the prevalence of these antidromic APs is of fundamental importance.

## 4. Methods

### 4.1. Microfluidic design and fabrication

The polydimethylsiloxane (PDMS) microfluidic chambers used in this study followed a design reported on our previous publications [31, 33], with minor optimizations regarding the number of

microchannels, as well as their length and width. The number of microchannels was reduced to match exactly the number of microelectrode columns (16 microchannels in total). The microchannel width was reduced to 10  $\mu\text{m}$  to isolate fewer axons per microchannel, thus decreasing the complexity of the recorded signals. The microchannel length was set to 700  $\mu\text{m}$  to selectively probe axonal function, as microchannels must be 450  $\mu\text{m}$  or greater in length to restrict the axonal compartment access to axons only [6, 57]. To maintain long-term axon viability throughout the whole microchannel length, we set the height to 10  $\mu\text{m}$ . This microchannel design accommodated for both types of axons under study (thinner hippocampal and thicker DRG axons) while maintaining the somata-exclusion capacity. Concisely, the microfluidic chambers were composed of two separate compartments (somal and axonal) interconnected by 16 microchannels with 700  $\mu\text{m}$  length  $\times$  10  $\mu\text{m}$  height  $\times$  10  $\mu\text{m}$  width dimensions and interspaced by 100  $\mu\text{m}$ . In specific imaging experiments, chambers with longer microchannels (1000  $\mu\text{m}$  length) and 200  $\mu\text{m}$  spacing were also used.

From the microfabricated SU-8 mold, the PDMS microfluidic chambers were produced by replica molding. PDMS was prepared using a 10:1 mix of silicone elastomer and its curing agent (Sylgard 184, Dow Corning) and degassed using a vacuum desiccator. Polymerization was achieved at 70  $^{\circ}\text{C}$  for 3 h, after which the PDMS microfluidic chambers were unmolded and cut. The medium reservoirs were manually punched with a steel biopsy punch ( $\varnothing$  6 mm). Microfluidic chambers used for cultures with DRG explants were adapted by adding an extra smaller reservoir ( $\varnothing$  3 mm), which allowed the seeding of the DRG in a central position, closer to the microchannels (as in [36, 58]).

### 4.2. $\mu\text{EF}$ preparation

$\mu\text{EF}$ s were prepared as previously detailed [31]. This method allowed for a reversible MEA/PDMS bonding (so that MEAs could be reused), but ensured a correct coupling since we did not observe any axonal outgrowth under the PDMS or medium leakage. Briefly, planar MEAs (Multi Channel Systems (MCS), Germany) of 252 titanium nitride recording microelectrodes (30  $\mu\text{m}$  in diameter) and four internal reference electrodes (organized in a 16 by 16 square grid) were air plasma-cleaned for 2 min at 90 W, shortly before the PDMS microfluidic chamber alignment. Then, both the MEAs and the microfluidic chambers were briefly submerged in 70% ethanol, allowed to air-dry inside a laminar flow hood, and sterilized by ultraviolet light exposure.  $\mu\text{EF}$  assembly was guided by a stereomicroscope, to correctly align the microchannels with the microelectrode grid. After alignment, the  $\mu\text{EF}$ s were allowed to air-dry and air plasma-cleaned for 2 min at 90 W for surface hydrophilization. The  $\mu\text{EF}$ s were then



sequentially coated with poly-D-lysine ( $20 \mu\text{g ml}^{-1}$ ) and laminin ( $5 \mu\text{g ml}^{-1}$ ) to promote cell adhesion. Each microchannel encompassed seven microelectrodes, as these were interspaced by  $100 \mu\text{m}$  (the first and last microelectrodes were at  $50 \mu\text{m}$  of the microchannel entry and exit point, respectively). Thin MEAs (tMEAs) with  $200 \mu\text{m}$  electrode interspacing were used in calcium imaging experiments, due to their compatibility with high-magnification objectives. When using tMEAs, longer microchannels ( $1000 \mu\text{m}$  length) with appropriate spacing were used to encompass five microelectrodes. A photograph of an assembled  $\mu\text{EF}$  is shown in figure 1(A).

### 4.3. Cell culture

Experimental procedures involving animals were carried out following current Portuguese laws on Animal Care (DL 113/2013) and the European Union Directive (2010/63/EU) on the protection of animals used for experimental and other scientific purposes. The experimental protocol (reference 0421/000/000/2017) was approved by the ethics committee of the Portuguese official authority on animal welfare and experimentation (Direção-Geral de Alimentação e Veterinária). All efforts were made to minimize the number of animals and their suffering.

Primary embryonic rat hippocampal neurons were isolated from Wistar rat embryos (E18) as in [31, 59]. Tissues were dissected in Hank's Balanced Salt Solution (HBSS) and enzymatically digested in 0.6% (w/v) trypsin (1:250) in HBSS for 15 min at  $37^\circ\text{C}$ . Then, trypsin was inactivated with culture medium containing 10% fetal bovine serum and washed away. Tissue fragments were mechanically dissociated with a plastic pipette and the cells' suspension was filtered with a  $40 \mu\text{m}$  strainer (Falcon) to exclude remaining tissue clumps. After cell counting, 150k viable cells suspended in  $5 \mu\text{l}$  were seeded in the somal compartment of the  $\mu\text{EF}$ . Cells were cultured in Neurobasal Plus medium supplemented with 0.5 mM glutamine, 2% (v/v) B27 Plus, and 1% (v/v) penicillin/streptomycin (P/S). For STED experiments, 75k viable cells were seeded on microfluidic chambers (with 700 or 1000  $\mu\text{m}$  long microchannels) assembled on  $22 \times 22 \text{ mm}$  glass coverslips (#1.5 thickness, Corning). These microfluidic chambers were peeled-off at one DIV and neurons were allowed to grow along the coated patterns (i.e. microchannels patterns). A total of 12 independent hippocampal cell preparations were performed for this study.

Primary embryonic mouse DRG explants were isolated from wild-type C57BL/6 mice embryos (E16.5) as in [36]. Lumbar DRG explants were removed and placed in HBSS until use. A single DRG explant was seeded in the somal compartment of each prepared  $\mu\text{EF}$ . Cells were cultured in Neurobasal medium supplemented with 0.5 mM glutamine, 2% (v/v) B27, 50 ng  $\text{ml}^{-1}$  of NGF 7 S (Calbiochem), and

1% (v/v) (P/S). A total of five independent DRG cell preparations were performed for this study.

For the experiments involving modulation of the DRG's distal axon biochemical environment, CM was obtained from bone resorbing osteoclasts. Bone resorbing osteoclasts were obtained via mouse bone marrow cells flushing. Pre-osteoclasts were obtained after three days of stimulation with macrophage colony-stimulating factor (M-CSF  $30 \text{ ng ml}^{-1}$ , PeproTech). Adherent cells were then detached and seeded on top of bone slices (boneslices.com, Denmark) in the presence of  $30 \text{ ng ml}^{-1}$  M-CSF and  $100 \text{ ng ml}^{-1}$  receptor activator of nuclear factor kappa-B ligand (RANKL, PeproTech) [36]. After four DIV, resorbing osteoclasts' secretome was collected, centrifuged at  $140 \text{ g}$ ,  $4^\circ\text{C}$ , 5 min, and stored at  $-80^\circ\text{C}$  before use.

All cultures were kept in a humidified incubator at  $37^\circ\text{C}$  supplied with 5%  $\text{CO}_2$ .

### 4.4. Viral transductions

Transductions with AAVs were performed to live-image neuronal morphology, axonal outgrowth and calcium imaging. For neuronal morphology, ssAAV-1/2-hCMV-chI-EGFP-WPRE-SV40p(A) ( $8.3 \times 10^{12} \text{ vg ml}^{-1}$  titer) or scAAV-DJ/2-hSyn1-chI-loxP-mRuby3-loxPSV40p(A) ( $7.2 \times 10^{12} \text{ vg ml}^{-1}$  titer) were added to the somal compartment ( $0.3 \mu\text{l}$  per  $\mu\text{EF}$  at one to five DIV). For performing calcium imaging of neurons extending to the axonal compartment, ssAAV-retro/2-hSyn1-chI-jGCaMP7f-WPRESV40p(A) ( $5.2 \times 10^{12} \text{ vg ml}^{-1}$  titer) was selectively added to the axonal compartment ( $0.5 \mu\text{l}$  per  $\mu\text{EF}$  at nine to ten DIV).

All viral vectors were produced by the Viral Vector Facility of the Neuroscience Center Zurich (Zentrum für Neurowissenschaften Zürich, ZNZ, Switzerland).

### 4.5. Electrophysiological recording

DRG explants at 6–11 DIV and hippocampal neurons at 11–25 DIV were used in the electrophysiology experiments. Before each recording session,  $\mu\text{EFs}$  were inspected for signs of contamination, poor cell viability or axonal degeneration (e.g. axonal blebbing). Inadequate  $\mu\text{EFs}$  were discarded. Recording sessions started after 5 min of adjustment to recording conditions. Electrophysiological recordings of spontaneous electrical activity were obtained at a sampling rate of 20 or 50 kHz for 5–15 or 1–2 min, respectively, unless otherwise specified. The high-temporal resolution recordings (at 50 kHz) were performed to obtain more precise calculations of conduction velocity and always took place after the longer 20 kHz recordings. All recordings were obtained using a commercial MEA2100-256 system (Multichannel Systems MCS, Germany). Temperature was maintained at  $37^\circ\text{C}$  by an external temperature controller. For long-term experiments (e.g. axonal activity modulation experiments), and whenever



imaging was performed concurrently, recordings were performed with the system mounted on an incubated (37 °C) inverted widefield microscope (Axiovert 200 M, Zeiss or Eclipse Ti2-E, Nikon) stage supplied with humidified 5% CO<sub>2</sub>.

#### 4.6. Axonal electrical stimulation and calcium imaging

Calcium imaging experiments were performed with hippocampal neurons at 18–21 DIV (at least one week post-transduction with AAV2-retro-jGCaMP7f). Images were acquired by a sCMOS camera Prime 95B, 22 mm (Teledyne Photometrics, UK), mounted on a Nikon Eclipse Ti2-E (Nikon, Japan) inverted microscope with a Nikon Achromatic ADI 10X/0.25NA, a Nikon Plan Apo 20X/0.75NA, or a Nikon Plan Apo LWD  $\lambda$  S 40X/1.15NA (water-immersion) objective. Image acquisition was performed using Micromanager (Version 1.4) at 200 Hz (5 ms exposure), which allowed for the temporal discrimination of soma depolarizations in response to single electrical pulse stimulations. Electrical stimulations were performed using the MEA2100-256 system's (MCS, Germany) internal stimulator. Per trial, five biphasic voltage pulses (−500/500 to −1000/1000 mV, 100  $\mu$ s per phase) were delivered to the last microelectrode within a microchannel at 0.5 or 1 Hz. To synchronize electrical stimulation, recording, and fast image acquisition, the whole setup was triggered via a transistor–transistor logic signal sent at the start of the MEA recording/stimulation protocol.

The resulting videos were median-filtered, regions of interest (i.e. somas, axons) were delineated manually and  $\Delta F/F_0$  traces were calculated in ImageJ using custom macros.  $\Delta F/F$  traces were exported for analysis in MATLAB 2018a (The Mathworks, Inc., USA).

#### 4.7. Axonal activity modulation

Distal axotomy was performed as previously described [57]. After a baseline recording, the medium from the axonal compartment was removed and stored for future use. Then, a pipette tip was placed at the entrance of the main channel and vacuum suction was applied. Axons were severed by the resulting air bubble that passed through the main channel. Then, the stored culture medium was returned to the axonal compartment. Axotomy was confirmed by imaging the whole culture pre- and post-axotomy.

For the selective blocking of activity, a medium pre-mixed with 1  $\mu$ M TTX, a potent fast voltage-gated sodium channels blocker, was added to the desired  $\mu$ EF compartment after removing and storing the original medium. A hydrostatic pressure difference was used to impair the flow of TTX between compartments. In the same recording session, we performed recordings before adding TTX (baseline), after adding to the axonal compartment, and after adding to the

somal compartment. At the end of the recording session, the exposed compartments were washed-out with three rounds of fresh medium replenishment and then allowed to equilibrate in the stored medium. A final recovery recording was performed on the following day.

Axonal stimulation through changes in the biochemical environment was tested in DRG cultures. For the modulation of the axon terminals' biochemical environment, osteoclast's CM was selectively applied to the axonal compartment as in [36]. First, a baseline recording of DRG cultures at six DIV was obtained. Afterward, the medium from the axonal compartment was gently aspirated and replaced by 100  $\mu$ l of osteoclast's CM. Post-treatment (0 h) recordings (20–30 min) were started as soon as the baseline stabilized following liquid flow perturbation (less than 1 min). Two post-treatment recordings (3 h and 24 h post-treatment) were performed additionally.

In all experiments, cultures were not moved out of the MEA2100-256 system during the experimental protocol of the day.

#### 4.8. Immunolabeling

Hippocampal neurons were fixed at six to seven DIV for STED imaging. Half the media was carefully aspirated and replaced by 4% PFA (2% final concentration) for 20 min at room temperature (RT). Then, the fixative was washed-out with three rounds of phosphate-buffered saline (PBS) 1 $\times$  and the fixed cells were permeabilized with 0.1% (v/v) triton X-100 (in PBS) for 5 min and autofluorescence was quenched with 0.2 M ammonium chloride (NH<sub>4</sub>Cl, in H<sub>2</sub>O). Non-specific labeling was blocked by incubation with blocking buffer (5% FBS in PBS 1 $\times$ ) for 1 h. Rabbit anti-Tau (GeneTex, cat# GTX130462, 1:1000) primary antibody diluted in blocking buffer was incubated for 1 h at RT. After three washes with PBS 1 $\times$ , incubation with secondary antibody (anti-rabbit Alexa Fluor® 488, Molecular Probes®, Thermo Fisher Scientific, 1:500) and 0.3  $\mu$ M phalloidin 635P (cat# 2-0205-002-5, Abberior GmbH, in PBS) for actin staining, was performed for 1 h at RT. After three washes with PBS 1 $\times$ , coverslips were mounted in 80% glycerol and sealed.

#### 4.9. STED imaging and analysis

STED imaging was performed in an Abberior Instrument 'Expert Line' gated-STED coupled to a Nikon Ti microscope with an oil-immersion 60  $\times$  1.4NA Plan-Apo objective (Nikon, Lambda Series) and a pinhole size set at 0.8 Airy units. The system features 40 MHz modulated excitation (405, 488, 560 and 640 nm) and depletion (775 nm) lasers. The microscope's detectors are avalanche photodiode detectors which were used to gate the detection between 700 ps and 8 ns. Typically, STED images were obtained near the entrance and exit of the microchannel patterns. After STED

imaging, microchannel regions were fully imaged in a widefield microscope (20× objective) for mapping of the culture topology. This allowed for the precise measure of the STED image localization, in relation to the microchannel length. Axons were identified based on the Tau specific staining and the presence of periodic actin rings within the membrane periodic skeleton. The diameter of axons focused on the maximum wide plan was measured manually. Per axon, at least five measures were acquired perpendicularly to the longitudinal axon axis by connecting the brighter outer pixels (most often actin rings).

#### 4.10. AP detection and propagation characterization

Raw signals were band-pass filtered (200–3000 Hz) and analyzed offline using custom MATLAB scripts. APs were detected by a threshold method set to  $4.5\text{--}6\times$  (DRG experiments) or  $6\times$  (hippocampal experiments) the standard deviation (STD) of the peak-to-peak electrode noise. An AP time was extracted at this surpassing point and no detection was considered for the next 2 ms ('dead time'). Events propagating along a microchannel were identified based on the extracted AP times. Propagation sequence identification and propagation velocity calculation were performed as previously reported [51] and the scripts are available in GitHub at [https://github.com/paulodecastroaguair/Calculate\\_AP\\_s\\_velocities\\_in\\_MEAs](https://github.com/paulodecastroaguair/Calculate_AP_s_velocities_in_MEAs).

For the hippocampal culture experiments, a propagating event had to fulfill the following requirements: event detected over the entire microchannel (seven microelectrodes); time delay between electrode pairs lower than or equal to 1 ms (minimum propagation velocity of  $0.1\text{ m s}^{-1}$ ); each AP time isolated, with no neighboring APs in a 4 ms time window. For the DRG culture experiments, due to the decrease in SNR at the extremities of the microchannels, we only considered the five inner electrodes of the microchannels for the forward/backward events ratios. The remaining requirements were kept the same. This stringent detection method profoundly reduced the number of possible propagating events, as it eliminated any ambiguity during bursts and excluded sequences with missing AP times on at least one microelectrode (supplementary figure S3). Due to the very high firing frequency observed during bursts, we consider interpretations from such instances as unclear: during bursts, it is very challenging to track specific APs (identity is lost); given the short inter-spike intervals in a burst, the conduction direction can be easily misperceived as being antidromic if the signal delay between electrodes is in the same order of magnitude as the inter-spike intervals (in an electrophysiology equivalent of the stroboscopic effect). Moreover, given the large number of axons per microchannel (figure 1(A)) and the longitudinal nature of the study (along multiple days),

we opted not to perform spike-sorting. Thus, we cannot ascertain if the detected propagating events per microchannel occurred in a single or in multiple synchronized axons.

For the propagation velocity calculations, the extracted AP times were further corrected based on the voltage waveforms. Each AP time, originally identified by the threshold method, was subject to a post-detection time correction (within a limited 1 ms window), allowing the AP time to assume the instant of the maximum absolute voltage of the signal trace. The corrected AP times ensured that the propagation velocity was calculated based on the reference APs' maximum absolute voltage (instead of the instant that the voltage profile crossed the threshold line). Propagation velocities per event were then calculated by dividing the first-to-last electrode distance ( $600\text{ }\mu\text{m}$  span) by the delay between AP times of the two electrodes (the first and last electrodes in the detected sequence).

Analysis of possible temporal correlations between AP times in different microchannels was carried out using a method very similar to the calculation of peristimulus time histograms. To assess the time dependence between antidromic APs in a particular microchannel (here called 'events') with the APs in all other microchannels, histograms of the time delays between each event and all APs times were calculated. The AP times were all obtained from a predefined reference electrode (the middle microelectrode) in each microchannel, and each histogram (one per microchannel) was calculated in a limited causal time window of 10 ms. Presumed antidromic APs consistently preceded by an AP in another microchannel would lead, using this method, to a pronounced peak in the histogram centered at the typical time delay between both.

#### 4.11. Simulations of conduction velocity in different axonal morphologies

Analysis of potential causes for asymmetric AP conduction was carried out in NEURON simulation environment [60] using a detailed biophysical model of an axon. The Hodgkin-Huxley formalism was used to describe ion conductances in the axon. Three currents were modeled: fast sodium and rectifying potassium currents responsible for APs in hippocampal neurons [61], and a leakage current supporting the resting potential. Default (original) parameters were used with the exception of: axial resistance  $R_a = 150\text{ }\Omega\text{ cm}^{-1}$ , leakage conductance  $g_L = 0.1\text{ mS cm}^{-2}$ , sodium conductance  $g_{Na} = 0.1\text{ S cm}^{-2}$ , and potassium conductance  $g_K = 0.1\text{ S cm}^{-2}$ . Simulations were carried out assuming a temperature of  $37\text{ }^\circ\text{C}$ . Two distinct overall morphologies were considered. In the first, the axon was modeled as a cylindrical structure with a length of 1 mm and a diameter of  $0.6\text{ }\mu\text{m}$ , with a spatial grid of  $10\text{ }\mu\text{m}$  (100 segments). Different diameter tapering levels were studied by keeping the somal end at  $0.6\text{ }\mu\text{m}$

and varying the diameter at the axonal terminal side. Tapering was quantified as the percentage of reduction in diameter in 1 mm distance. In the second morphology, branching was considered. The axon was still modeled as a cylindrical structure but now branching every 250  $\mu\text{m}$  for a full total length of 1 mm on each of the eight branches. After each branch node the axon diameter was allowed to be reduced. As with tapering, this reduction quantified as the percentage of reduction in diameter in 1 mm distance ( $\% \text{mm}^{-1}$ ). In both morphologies, conduction velocity was calculated for both propagation directions by providing stimulation (at rheobase level, for 1 ms) at either axonal end.

#### 4.12. FEM of the electrical potential inside the microchannels

The tridimensional (3D) FEM geometry replicating the  $\mu\text{EF}$  microchannels, was constructed with SOLIDWORKS software (v. 2018, Dassault Systemes SolidWorks Corporation, France). The dimensions' details for all components of the model are available in supplementary table 1. Finite element analysis was performed with the AC/DC module of the COMSOL Multiphysics software (v. 5.2a, Stockholm, Sweden). The electric current physics interface was selected, considering a transient time-dependent study. A 3D model physics-controlled mesh was also generated in COMSOL for the constructed MEA 3D geometry model, with the extremely fine mesh option. This model is composed of 13 different domains, whose description, number and electrical properties are available in supplementary table 2. Electrical boundary conditions were added to the model: two ground conditions at each of the culture medium domain extremities, and an electric potential boundary condition added to each of the axons' surfaces. The axon's boundary condition served the purpose of recreating, in global terms, the biphasic profile observed in extracellular recordings. The derivative of a Gaussian function was used here as the biphasic profile. Instead of stationary, the center of the Gaussian function in the axon's boundary condition was made to depend on time, introducing a wave motion that propagates the entire axon length.

Two different studies were carried, each corresponding to the AP traveling across one of the two axons. Domain probes were added to all of the electrodes to gather the predicted average electric potential in each time-step for each study solution. The direct solver NUMPS was used for both studies.

#### 4.13. Inclusion criteria and statistical analyses

Electrodes with an MFR of at least 0.1 Hz were considered as 'active electrodes'. We defined as 'active microchannels' those that had at least one detected propagating event per recording. In the stringent conditions of our conduction detection algorithm, propagating events require consistent readouts in all

microelectrodes in the microchannel. Consequently, it is important to note that the number of detected propagating events per microchannel did not necessarily correlate with the firing rate. Moreover, the propagating event detection method excluded most APs within bursts (supplementary figure S3), as these could lead to ambiguous detections of propagation direction. As the total number of detected propagating events could vary greatly across days within the same microchannel/ $\mu\text{EF}$  (although their direction flow was generally maintained), we opted for characterizing the ratio of antidromic/orthodromic activity in relative fractions for the analyses of the axotomy and chemical blocking/stimulation experiments. All statistical data is presented as mean  $\pm$  STD, unless otherwise specified. Sample sizes and used tests are indicated in the figures' legends or in the main text. Statistical significance was considered for  $p < 0.05$ . A summary of the dataset of hippocampal and DRG  $\mu\text{EF}$  experiments is shown in supplementary tables 3 and 4, respectively.

#### Data availability statement

The data that support the findings of this study are openly available at the following URL/DOI: [10.5281/zenodo.5745978](https://doi.org/10.5281/zenodo.5745978).


#### Acknowledgments

This work was partially financed by FEDER—Fundo Europeu de Desenvolvimento Regional funds through the COMPETE 2020—Operational Programme for Competitiveness and Internationalisation (POCI), Portugal 2020, and by Portuguese funds through FCT—Fundação para a Ciência e a Tecnologia/Ministério da Ciência, Tecnologia e Ensino Superior in the framework of the projects PTDC/EMD-EMD/31540/2017 (POCI-01-0145-FEDER-031540) and PTDC/MED-NEU/28623/2017 (NORTE-01-0145-FEDER-028623). We thank Alla Karpova from the Janelia Virus Service Facility (HHMI Janelia Research Campus) for providing the AAV-retro vector. All the members of the Neuroengineering and Computational Neuroscience (NCN) group for help and critical discussions. NCN alumni, especially Kristine Heiney, for help and critical discussions. Sean Weaver (ETH Zurich) for critical discussions. Hélder Maiato and António Pereira (Chromosome Instability and Dynamics, IBMC/i3S) for support in STED microscopy. We acknowledge the support of the i3S Scientific Platform Bioimaging, member of the national infrastructure PPBI—Portuguese Platform of Bioimaging (PPBI-POCI-01-0145-FEDER-022122). J C M was supported by FCT (PD/BD/135491/2018) in the scope of the BiotechHealth PhD Program (Doctoral Program on Cellular and Molecular Biotechnology Applied to Health Sciences). M A was supported by

FCT through the Scientific Employment Stimulus (CEECIND/03415/2017).

## ORCID iDs

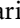
JC Mateus  <https://orcid.org/0000-0001-8058-5093>

CDF Lopes  <https://orcid.org/0000-0002-7467-6498>

M Aroso  <https://orcid.org/0000-0002-3118-0185>

A Gerós  <https://orcid.org/0000-0003-4585-0351>

E Neto  <https://orcid.org/0000-0003-2334-2292>

M Lamghari  <https://orcid.org/0000-0002-2500-4548>

MM Sousa  <https://orcid.org/0000-0002-4524-2260>

P Aguiar  <https://orcid.org/0000-0003-4164-5713>

## References

- [1] Alcami P and El Hady A 2019 Axonal computations *Front. Cell Neurosci.* **13** 413
- [2] Debanne D, Campanac E, Bialowas A, Carlier E and Alcaraz G 2011 Axon physiology *Physiol. Rev.* **91** 555–602
- [3] Chéreau R, Saraceno G E, Angibaud J, Cattaert D and Nägerl U V 2017 Superresolution imaging reveals activity-dependent plasticity of axon morphology linked to changes in action potential conduction velocity *Proc. Natl Acad. Sci. USA* **114** 1401–6
- [4] Peterka D S, Takahashi H and Yuste R 2011 Imaging voltage in neurons *Neuron* **69** 9–21
- [5] Sasaki T, Matsuki N and Ikegaya Y 2011 Action-potential modulation during axonal conduction *Science* **331** 599–601
- [6] Neto E et al 2016 Compartmentalized microfluidic platforms: the unrivaled breakthrough of *in vitro* tools for neurobiological research *J. Neurosci.* **36** 11573–84
- [7] Holloway P M et al 2021 Advances in microfluidic *in vitro* systems for neurological disease modeling *J. Neurosci. Res.* **99** 1276–307
- [8] Emmenegger V, Obien M E J, Franke F and Hierlemann A 2019 Technologies to study action potential propagation with a focus on HD-MEAs *Front. Cell Neurosci.* **13** 159
- [9] Sasaki T 2013 The axon as a unique computational unit in neurons *Neurosci. Res.* **75** 83–88
- [10] Traub R D, Whittington M A, Maier N, Schmitz D and Nagy J I 2020 Could electrical coupling contribute to the formation of cell assemblies? *Rev. Neurosci.* **31** 121–41
- [11] Bucher D and Goaillard J-M 2011 Beyond faithful conduction: short-term dynamics, neuromodulation, and long-term regulation of spike propagation in the axon *Prog. Neurobiol.* **94** 307–46
- [12] Hodgkin A L and Huxley A F 1952 A quantitative description of membrane current and its application to conduction and excitation in nerve *J. Physiol.* **117** 500–44
- [13] Pinault D 1995 Backpropagation of action potentials generated at ectopic axonal loci: hypothesis that axon terminals integrate local environmental signals *Brain Res. Rev.* **21** 42–92
- [14] Dugladze T, Schmitz D, Whittington M A, Vida I and Gloveli T 2012 Segregation of axonal and somatic activity during fast network oscillations *Science* **336** 1458–61
- [15] Chorev E and Brecht M 2012 *In vivo* dual intra- and extracellular recordings suggest bidirectional coupling between CA1 pyramidal neurons *J. Neurophysiol.* **108** 1584–93
- [16] Bähner F et al 2011 Cellular correlate of assembly formation in oscillating hippocampal networks *in vitro Proc. Natl Acad. Sci. USA* **108** 35
- [17] Bukalo O, Campanac E, Hoffman D A and Fields R D 2013 Synaptic plasticity by antidromic firing during hippocampal network oscillations *Proc. Natl Acad. Sci. USA* **110** 5175–80
- [18] Thome C, Roth F C, Obermayer J, Yanez A, Draguhn A and Egorov A V 2018 Synaptic entrainment of ectopic action potential generation in hippocampal pyramidal neurons *J. Physiol.* **596** 5237–49
- [19] Sheffield M E J, Best T K, Mensh B D, Kath W L and Spruston N 2011 Slow integration leads to persistent action potential firing in distal axons of coupled interneurons *Nat. Neurosci.* **14** 200–7
- [20] Stasheff S F, Hines M and Wilson W A 1993 Axon terminal hyperexcitability associated with epileptogenesis *in vitro*. I. Origin of ectopic spikes *J. Neurophysiol.* **70** 961–75
- [21] Hamada M S and Mhp K 2015 Myelin loss and axonal ion channel adaptations associated with gray matter neuronal hyperexcitability *J. Neurosci.* **35** 7272–86
- [22] Gutnick M J and Prince D A 1972 Thalamocortical relay neurons: antidromic invasion of spikes from a cortical epileptogenic focus *Science* **176** 424–6
- [23] Bukalo O, Lee P R and Fields R D 2016 BDNF mRNA abundance regulated by antidromic action potentials and AP-LTD in hippocampus *Neurosci. Lett.* **2** 97–102
- [24] Schmitz D et al 2001 Axo-axonal coupling: a novel mechanism for ultrafast neuronal communication *Neuron* **31** 831–40
- [25] Anastassiou C A, Perin R, Markram H and Koch C 2011 Ephaptic coupling of cortical neurons *Nat. Neurosci.* **14** 217–23
- [26] Han K-S, Guo C, Chen C H, Witter L, Osorno T and Regehr W G 2018 Ephaptic coupling promotes synchronous firing of cerebellar Purkinje cells *Neuron* **100** 564–578.e3
- [27] Whittington J C R and Bogacz R 2019 Theories of error back-propagation in the brain *Trends Cogn. Sci.* **23** 235–50
- [28] Rumelhart D E, Hinton G E and Williams R J 1986 Learning representations by back-propagating errors *Nature* **323** 533–6
- [29] Black B J et al 2019 Emerging neurotechnology for antinoceptive mechanisms and therapeutics discovery *Biosens. Bioelectron.* **126** 679–89
- [30] Nascimento A I, Mar F M and Sousa M M 2018 The intriguing nature of dorsal root ganglion neurons: linking structure with polarity and function *Prog. Neurobiol.* **168** 86–103
- [31] Lopes C D F, Mateus J C and Aguiar P 2018 Interfacing microfluidics with microelectrode arrays for studying neuronal communication and axonal signal propagation *J. Vis. Exp.* **142** 1–8
- [32] Lewandowska M K, Radivojević M, Jäckel D, Müller J and Hierlemann A R 2016 Cortical axons, isolated in channels, display activity-dependent signal modulation as a result of targeted stimulation *Front. Neurosci.* **10** 83
- [33] Heiney K, Mateus J C, Lopes C D F, Neto E, Lamghari M and Aguiar P 2019  $\mu$ SpikeHunter: an advanced computational tool for the analysis of neuronal communication and action potential propagation in microfluidic platforms *Sci. Rep.* **9** 5777
- [34] Habibey R, Latifi S, Mousavi H, Pesce M, Arab-Tehrany E and Blau A 2017 A multielectrode array microchannel platform reveals both transient and slow changes in axonal conduction velocity *Sci. Rep.* **7** 8558
- [35] Moutaux E, Charlot B, Genoux A, Saudou F and Cazorla M 2018 An integrated microfluidic/microelectrode array for the study of activity-dependent intracellular dynamics in neuronal networks *Lab Chip* **18** 3425–35
- [36] Neto E et al 2020 Sensory neurons sprouting is dependent on osteoclast-derived extracellular vesicles involving the activation of epidermal growth factor receptors *bioRxiv* (<https://doi.org/10.1101/259218>)
- [37] Pan L, Alagapan S, Franca E, DeMarse T, Brewer G J and Wheeler B C 2014 Large extracellular spikes recordable from



- axons in microtunnels *IEEE Trans. Neural. Syst. Rehabil. Eng.* **22** 453–9
- [38] Tervo D G R *et al* 2016 A designer AAV variant permits efficient retrograde access to projection neurons *Neuron* **92** 372–82
- [39] Dana H *et al* 2019 High-performance calcium sensors for imaging activity in neuronal populations and microcompartments *Nat. Methods* **16** 649–57
- [40] Shrirao A B *et al* 2018 Microfluidic platforms for the study of neuronal injury *in vitro* *Biotechnol. Bioeng.* **115** 815–30
- [41] Costigan M, Scholz J and Woolf C J 2009 Neuropathic pain: a maladaptive response of the nervous system to damage *Annu. Rev. Neurosci.* **32** 1–32
- [42] Amir R, Kocsis J D and Devor M 2005 Multiple interacting sites of ectopic spike electrogenesis in primary sensory neurons *J. Neurosci.* **25** 2576–85
- [43] Hiasa M *et al* 2017 Bone pain induced by multiple myeloma is reduced by targeting V-ATPase and ASIC3 *Cancer Res.* **77** 1283–95
- [44] Waxman S G 1980 Determinants of conduction velocity in myelinated nerve fibers *Muscle Nerve* **3** 141–50
- [45] Goldstein S S and Rall W 1974 Changes of action potential shape and velocity for changing core conductor geometry *Biophys. J.* **14** 731–57
- [46] Hu W, Tian C, Li T, Yang M, Hou H and Shu Y 2009 Distinct contributions of Nav1.6 and Nav1.2 in action potential initiation and backpropagation *Nat. Neurosci.* **12** 996–1002
- [47] Yuan X *et al* 2020 Versatile live-cell activity analysis platform for characterization of neuronal dynamics at single-cell and network level *Nat. Commun.* **11** 4854
- [48] Bakkum D J *et al* 2013 Tracking axonal action potential propagation on a high-density microelectrode array across hundreds of sites *Nat. Commun.* **4** 2181
- [49] Costa A R, Pinto-Costa R, Sousa S C and Sousa M M 2018 The regulation of axon diameter: from axonal circumferential contractility to activity-dependent axon swelling *Front. Mol. Neurosci.* **11** 319
- [50] Xu K, Zhong G and Zhuang X 2013 Actin, spectrin, and associated proteins form a periodic cytoskeletal structure in axons *Science* **339** 452–6
- [51] Costa A R *et al* 2020 The membrane periodic skeleton is an actomyosin network that regulates axonal diameter and conduction *eLife* **9** e55471
- [52] Gladkov A *et al* 2017 Design of cultured neuron networks *in vitro* with predefined connectivity using asymmetric microfluidic channels *Sci. Rep.* **7** 15625
- [53] Sakai K, Shimba K, Kotani K and Jimbo Y 2017 A co-culture microtunnel technique demonstrating a significant contribution of unmyelinated Schwann cells to the acceleration of axonal conduction in Schwann cell-regulated peripheral nerve development *Integr. Biol.* **9** 678–86
- [54] Tsantoulas C, Farmer C, Machado P, Baba K, McMahon S B and Raouf R 2013 Probing functional properties of nociceptive axons using a microfluidic culture system *PLoS One* **8** e80722
- [55] Enes J *et al* 2010 Electrical activity suppresses axon growth through Cav1.2 channels in adult primary sensory neurons *Curr. Biol.* **20** 1154–64
- [56] Aebbersold M J *et al* 2016 ‘Brains on a chip’: towards engineered neural networks *TrAC—Trends Anal. Chem.* **78** 60–69
- [57] Park J W, Vahidi B, Taylor A M, Rhee S W and Jeon N L 2006 Microfluidic culture platform for neuroscience research *Nat. Protocols* **1** 2128–36
- [58] Neto E *et al* 2014 Sensory neurons and osteoblasts: close partners in a microfluidic platform *Integr. Biol.* **6** 586–95
- [59] Mateus J C *et al* 2019 Improved *in vitro* electrophysiology using 3D-structured microelectrode arrays with a micro-mushrooms islets architecture capable of promoting topotaxis *J. Neural Eng.* **16** 036012
- [60] Hines M L and Carnevale N T 1997 The NEURON simulation environment *Neural Comput.* **9** 1179–209
- [61] Traub R D and Miles R 1991 *Neuronal Networks of the Hippocampus* (Cambridge: Cambridge University Press)